Planetary and Space Science 58 (2010) 1857–1867

Contents lists available at ScienceDirect

Planetary and Space Science

journal homepage: www.elsevier.com/locate/pss

Two-dimensional time-dependent model of the transport of minor species in the Venus night side upper atmosphere

Arnaud Collet *,[1], Cédric Cox, Jean-Claude Gérard

Laboratoire de Physique Atmosphérique et Planétaire, Université de Liège, Belgium

ARTICLE INFO

Article history:
Received 28 May 2010
Received in revised form
2 August 2010
Accepted 16 August 2010
Available online 22 August 2010

Keywords:
Venus atmosphere
Transport
Nightglow
Numerical modelling

ABSTRACT

We present a numerical tool developed to quantify the role of processes controlling the spatio-temporal distribution of the NO ultraviolet and $O_2(^1\Delta_g)$ infrared nightglows in the Venus night side upper atmosphere, observed with the VIRTIS and SPICAV instruments on board Venus Express. This numerical tool consists in a two-dimensional chemical-transport time-dependent model which computes in a hypothetical rectangular solving domain the spatio-temporal distributions of the number densities of the four minor species at play in these two nightglow emissions. The coupled nonlinear system of the four partial differential equations, describing the spatio-temporal variations of the minor species, has been solved using a finite volume method with a forward Euler method for the time integration scheme. As an application, we have first simulated a time-constant supply of atoms through the upper boundary of the solving domain. The fluxes are inhomogeneous relative to its horizontal direction, in order to simulate regions of enhanced downward flow of oxygen and nitrogen giving rise to NO and O_2 brightening. Given that these two emissions show large time variations, we have also simulated a time-dependent downward flux of O and N atoms. It results from these simulations that the lack of correlation between the NO and $O_2(^1\Delta_g)$ nightglows largely result from to the coupling between horizontal and vertical transport processes and the very different chemical lifetimes of the two species. In particular, we have quantified the role of each process generating spatio-temporal de-correlations between the NO and $O_2(^1\Delta_g)$ nightglows.

1. Introduction

The study of airglow has been extensively used to remotely probe the chemical composition, temperature structure and dynamical characteristics of planetary atmospheres. The FUV Venus night side airglow is dominated by the presence of the δ and γ bands of nitric oxide extending between 180 and 310 nm. The emission is produced by radiative recombination through inverse pre-association of nitrogen $N(^4S)$ and oxygen $O(^3P)$ atoms. The sequence of processes may be written:

$$N + O \longrightarrow NO(C^2\Pi), \quad (1)$$

followed by

$$NO(C^2\Pi) \longrightarrow NO(X^2\Pi) + \delta\text{-bands} \quad (2)$$

and

$$NO(A^2\Sigma, v' = 0) \longrightarrow NO(X^2\Pi) + \gamma\text{-bands}. \quad (3)$$

The N and O atoms are produced on the dayside by dissociation of N_2 and CO_2 by extreme ultraviolet (EUV) solar photons and by photoelectron impact. They are carried from the day to the night side by the subsolar to antisolar circulation where they recombine. The NO airglow emission is highly variable in brightness and morphology over consecutive 24-hours periods as was shown by Stewart et al. (1980). The location of the brightest spot ranged from 2130 to 0300 LT and 39°S to 60°N (Bougher et al., 1990) and appeared to vary erratically. Stewart et al. (1980) built up a global map by combining 35 daily maps of the Venus nightside of the NO nightglow. This statistical map shows that the emission forms a bright spot which is shifted from the antisolar point toward dawn by approximately 2 h and about 10°–20° south of the equator. The emission rate of this bright region is $\sim 1.9 \pm 0.6$ kilo-Rayleighs (kR) in the (0, 1) delta band with an average hemispheric nightside intensity of 0.48 kR (Bougher et al., 1990). The shift of this statistical bright spot was interpreted as an indication of the presence of a super-rotation wind component at or above the altitude of the NO emission peak. The altitude of the emission peak was determined from PV-OUVS observations from periapsis by Gérard et al. (1981) who concluded that the emission peak is located at 115 ± 2 km. A much larger set of limb observations of the NO δ and γ bands nightglow was made with the SPICAV ultraviolet spectrometer (Bertaux et al., 2007) on board Venus

* Corresponding author. Tel.: +32 4 3663356.
E-mail address: A.Collet@ulg.ac.be (A. Collet).
[1] Fellowship Beneficiary—Research Training Fund for Industry and Agriculture. Now at Laboratoire de Thermodynamique des Phénomènes Irréversibles, Université de Liège, Belgium.

0032-0633/$ - see front matter © 2010 Elsevier Ltd. All rights reserved.
doi:10.1016/j.pss.2010.08.016

Express. The mean altitude of the emission layer was found to be located at 113 ± 5.8 km. The limb brightness of the NO emission is very variable, with peak intensities values below 5 kR at northern mid-latitudes, up to 440 kR at lower latitudes (Gérard et al., 2008a). The mean altitude of the emission peak statistically drops with increasing latitude between 6° and 72°N.

The oxygen airglow (0–0) band at 1.27 μm belongs to the $a^1\Delta_g \longrightarrow X^3\Sigma_g$ Atmospheric Infrared system has a radiative lifetime of about 70 min. (Miller et al., 2001). It was first identified in ground-based spectra of Venus by Connes et al. (1979). Subsequent ground-based telescope observations (Allen et al., 1992; Crisp et al., 1996; Lellouch et al., 1997; Ohtsuki et al., 2008; Bailey et al., 2008) have indicated that the oxygen IR nightglow is patchy, highly variable on timescales as short as 1 h. It is produced by recombination of oxygen atoms transported to the nightside by the global thermospheric circulation where they recombine in three-body collisions. Below ~ 90 km, the $O_2(a^1\Delta_g)$ molecules are deactivated by collisions with CO_2. Based on VIRTIS-M O_2 airglow limb observations, Drossart et al. (2007) determined that the O_2 peak emission is located near 96 km. Gérard et al. (2009) analyzed emission limb profiles extracted from VIRTIS limb images. They found that the peak altitude of the $O_2(^1\Delta_g)$ volume emission rate is typically located between 95 and 100 km, with a mean value of 97.4 ± 2.5 km. A similar conclusion was reached by Piccioni et al. (2009). Observations by VIRTIS in the nadir mode have been used to construct statistical maps of the Venus atmosphere in the O_2 emission band (Gérard et al., 2008b; Piccioni et al., 2009). These maps indicate the region of enhanced emission is centered on the antisolar point. The role of horizontal transport on the $O_2(^1\Delta_g)$ airglow distribution was analyzed by Hueso et al. (2008) who found that the O_2 nightglow nadir intensity is highly inhomogeneous. Regions of highest intensity are generally observed at low latitudes near midnight. They showed that the zonal wind is dominated by an intense prograde jet from dawn to midnight extending up to 22 h in local time, with lower velocities and reversed sign from dusk. The brightest small-scale (~ 100 km) features appeared correlated with locations of apparent convergence which may be a signature of compression and downwelling. The lack of homogeneity and the time variations observed in the $O_2(^1\Delta_g)$ nightglow indicate that the distribution of the downward flow of oxygen and nitrogen atoms is also time-dependent. These time effects are a possibly generated by variations in the global circulation due to changes in eddy transport efficiency and gravity wave breaking (Bougher et al., 2006).

The concept of production of O and N atoms followed by transport to the nightside by the subsolar to antisolar circulation, downward turbulent mixing and radiative recombination was validated by three-dimensional simulations using the Venus Thermospheric General Circulation Model (VTGCM) (Bougher et al., 1990). The statistical location of the NO airglow bright spot was reasonably well predicted by the three-dimensional model and implied zonal winds of about 50–75 m s^{-1} in the 115–150 km region. Gérard et al. (2009) analyzed concurrent observations of the NO and $O_2(^1\Delta_g)$ airglow emissions in the nadir direction with Venus Express. They showed that a low degree of correlation is observed between the two emissions observed quasi-simultaneously. Additionally, their statistical study has demonstrated that no correlation is observed between the variations of the altitude and the intensity of the two airglow emissions simultaneously observed in the grazing limb geometry. In summary, the de-correlation between the two emissions is based on three different sets of observations:

- the statistical location of the NO and the $O_2(^1\Delta_g)$ regions of enhanced emission are not coincident;
- nadir quasi-simultaneous nadir observations of the two emissions demonstrate that the distribution of the intensity along latitudinal cuts exhibits significant differences;
- limb observations indicate that neither the brightness nor the altitude of the emission peak co-vary in the northern hemisphere.

Gérard et al. (2009) suggested that the airglow de-correlation is a consequence of the transport of the downward moving air mass by horizontal winds in the transition region. As a result, zones of bright O_2 airglow regions are displaced along the wind direction from the source region of enhanced O and N downward flux and NO emission. A crude calculation indicated that the O atoms may move over considerable horizontal distances during the transit time needed to travel down the 15 km separating the two airglow layers. For a horizontal wind velocity value of 10 m s^{-1}, they estimated a typical horizontal transport range of ~ 800 to 5300 km. However, such estimates neglect the effects of the finite chemical lifetime of the O and N atoms which chemically recombine along their trajectory.

To quantitatively address the question of the role of horizontal transport on inhomogeneities in the Venus nightside airglow, a numerical model coupling the O and N photochemistry with transport is needed. This study describes the concept, numerical method and illustrates results obtained with such a two-dimensional model. First, we introduce the model equations to numerically solve and we roughly examine the time scales of the different processes at play. Then, we present the numerical method used to develop the two-dimensional time-dependent model. Second, we show steady state and time-dependent solutions obtained from this model and we discuss the different results. Finally, we draw some conclusions about this study.

2. Two-dimensional time-dependent model

2.1. The model equations

In this study, we focus on the spatio-temporal evolution of the number densities of four minor species on the night side of the atmosphere of Venus: atomic oxygen, atomic nitrogen, nitric oxide and excited molecular oxygen in the $O_2(^1\Delta_g)$ singlet state. We consider these species because they control the spatio-temporal behavior of the infrared and ultraviolet nightglows through a series of physical and chemical processes.

In order to develop the 2D time-dependent model, it has been assumed that the temperature and velocity fields are prescribed everywhere at any time inside the solving domain. Therefore, we do not solve the energy and momentum equations as in a full hydrodynamical solution. Consequently, the only equation is the continuity equation for each studied species:

$$\frac{\partial n_i}{\partial t} = -\vec{\nabla}.\vec{\Phi}^{\,i}_{adv} - \vec{\nabla}.\vec{\Phi}^{\,i}_{diff} + P_i - L_i, \tag{4}$$

where n_i is the number density of the minor species i, $\vec{\Phi}_{adv,i}$ is its advective flux and $\vec{\Phi}_{diff,i}$ the diffusive flux i, P_i and L_i represent, respectively, the chemical production and loss rates of minor species i. Additional assumptions have been made to develop the numerical model. First, we assumed that all quantities only depend on two independent spatial variables. We define an ideal rectangular solving domain in order to study the relative importance of the different physical and chemical processes taking place in the Venus upper atmosphere. This model is not a realistic description of the atmosphere of Venus. Instead, it must be viewed as a numerical tool to investigate the competition between different processes occurring in the atmosphere of Venus

and estimate the relative role and timescale of the various mechanisms at play. It is important to note that the objectives of this numerical tool are quite different from those of general circulation models (GCMs) such as the VTGCM. The two-dimensional time-dependent model, presented in this study, is a local model. Consequently, we have the possibility to adopt a better spatial resolution than the VTGCM. Moreover, the VTGCM solves the full hydrodynamical problem whereas our numerical tool only solves the continuity equation for each considered species. As a consequence, that gives the opportunity to investigate the influence of the prescribed fields (temperature, velocity) on the results, unlike the VTGCM where these fields are calculated from basic equations. The VTGCM is used to study steady state solutions whereas our model has been developed to investigate time-dependent behaviors. So, it clearly appears that the VTGCM and our model are very different and have been developed for different goals.

A Cartesian coordinate system has been used so as to locate the position in the solving domain. The x and z coordinates determine the position following the horizontal and vertical directions in the solving domain, respectively. In addition, diffusion processes along the horizontal direction has been neglected because it is very weak in comparison with advection in this same direction. Horizontal advection has been explicitly taken into account in the model. As for vertical advection, it is simulated by the diffusion term as explained further in this study. Moreover, the temperature field is assumed to be homogeneous relative to the x coordinate. Indeed, we have noted, due to the one-dimensional chemical-diffusive model developed by Gérard et al. (2008a), that the dependence of the temperature field on the local time does not considerably affect the obtained solution. The vertical temperature distribution used in the model has been taken from the empirical VTS3 model (Hedin et al., 1983). The velocity field $\vec{v}$ is prescribed everywhere at all times in the two-dimensional solving domain. It must satisfy the continuity equation relative to the total number density n, in the domain:

$$\frac{\partial n}{\partial t} = -\vec{\nabla}.(n\vec{v}). \tag{5}$$

Consequently, the velocity field used in the numerical model cannot be chosen in an arbitrary way. Given that the total number density of the Venusian atmosphere is considered as stationary, we can reasonably assume that $\partial n/\partial t = 0$. Moreover, if n is considered as uniform along the x coordinate, the total number density only depends on the z coordinate. Now, Eq. (5) can be cast in the form:

$$n(z)\frac{\partial u(x,z)}{\partial x} + n(z)\frac{\partial w(x,z)}{\partial z} + w(x,z)\frac{\partial n(z)}{\partial z} = 0, \tag{6}$$

where $u(x, z)$ and $w(x, z)$ represent the horizontal and vertical components of the velocity field, respectively. As mentioned previously, the actual spatial distribution of the velocity components is not known with accuracy. In addition, the velocity field must satisfy equation (6). In order to verify Eq. (6), we have assumed that the horizontal velocity component u only depends on the independent variable z whereas the vertical component w is taken as equal to zero, although, the actual vertical advection in the Venus thermosphere is not null. The effect of vertical advection is implicitly simulated by eddy diffusion with an altitude dependent coefficient K. A similar method was adopted by several authors in earlier studies (Roble and Gary, 1979; Gérard et al., 2008a) of minor constituent thermospheric transport. Taking these assumptions into account, Eq. (4) can be cast as

$$\frac{\partial n_i}{\partial t} = -\frac{\partial(\Phi^i_{adv})_x}{\partial x} - \frac{\partial(\Phi^i_{diff})_z}{\partial z} + P_i - L_i, \tag{7}$$

where the vertical diffusive flux $(\Phi^i_{diff})_z$ of a minor constituent is given by (Colegrove et al., 1965)

$$(\Phi^i_{diff})_z = (\Phi^i_{mol.diff.})_z + (\Phi^i_{edd.diff.})_z = -(D_i + K)\left(\frac{\partial n_i}{\partial z} + \frac{n_i}{T}\frac{\partial T}{\partial z}\right) - \left(\frac{D_i}{H_i} + \frac{K}{H}\right)n_i, \tag{8}$$

with D_i the molecular diffusion coefficient for constituent i, K is the vertical eddy diffusion coefficient, H_i is the local scale height of the ith constituent, H is the atmospheric scale height and T is the neutral gas temperature. We adopt a vertical distribution of the eddy diffusion coefficient K similar to that used in earlier studies (von Zahn et al., 1979), that is

$$K(z) = \frac{A}{\sqrt{n(z)}}\ \mathrm{cm^2\ s^{-1}}, \tag{9}$$

where A is a parameter of the model independent of the z coordinate. Moreover, as seen in relation (9), K is identical for all constituents and only depends on the z coordinate. The molecular diffusion coefficient D_i for the constituent i is given by (Banks and Kockarts, 1973)

$$D_i(z) = 1.52 \times 10^{18}\frac{\sqrt{T(z)\left(\frac{m_0}{m} + \frac{m_0}{m_i}\right)}}{n(z)}\ \mathrm{cm^2\ s^{-1}}, \tag{10}$$

with CO_2 taken as the background gas and where m_0, m and m_i are, respectively, the mass of a hydrogen atom, the molecular weight and the mean molecular mass of the Venusian atmosphere. The horizontal advective flux $(\Phi^i_{adv})_x$ is simply given by the $u \times n_i$ product. The chemical production P_i and loss L_i rates reflect the effect of chemical reactions taken into account in the model. We consider the following set of chemical reactions (Table 1):

$$N + O \xrightarrow{k_1} NO + h\nu_{UV}, \tag{11}$$

$$N + O + CO_2 \xrightarrow{k_2} NO + CO_2, \tag{12}$$

$$N + NO \xrightarrow{k_3} N_2 + O, \tag{13}$$

$$O + O + CO_2 \xrightarrow{k_4} O_2^{\star} + CO_2, \tag{14}$$

$$O_2(^1\Delta_g) + CO_2 \xrightarrow{k_5} O_2 + CO_2^{\star}, \tag{15}$$

$$O_2(^1\Delta_g) \xrightarrow{k_6} O_2 + h\nu_{IR}. \tag{16}$$

Table 1
Rate coefficients of chemical reactions.

Reaction	Rate	Reference
(11)	$k_1 = 1.92 \times 10^{-17} \times (300/T)^{1/2} \times (1-0.57/T^{1/2})\ \mathrm{cm^3\ s^{-1}}$	Dalgarno et al. (1992)[a]
(12)	$k_2 = 2 \times 10^{-32} \times (300/T)^{1/2}\ \mathrm{cm^6\ s^{-1}}$	Campbell and Thrush (1966)[b]
(13)	$k_3 = 2.5 \times 10^{-10} \times (T/300)^{1/2} \times \exp(-600/T)\ \mathrm{cm^3\ s^{-1}}$	Fox (1994)[a]
(14)	$k_4 = 2.8 \times 10^{-32}\ \mathrm{cm^6\ s^{-1}}$	Campbell and Gray (1973)[b]
(15)	$k_5 = 3 \times 10^{-20}\ \mathrm{cm^3\ s^{-1}}$	Yung and Demore (1982)[b]
(16)	$k_6 = 2.38 \times 10^{-4}\ \mathrm{s^{-1}}$	Miller et al. (2001)[b]

[a] Determined from observational and modelling works.
[b] Experimentally determined.

Now, all terms in Eq. (7) are known in an explicit way. Eq. (7) may be written in the quasi-linear form:

$$\frac{\partial n_i}{\partial t} = A_i \frac{\partial^2 n_i}{\partial z^2} + B_i \frac{\partial n_i}{\partial z} + C_i \frac{\partial n_i}{\partial x} + E_i n_i + P_i - L_i \quad \forall i = \mathrm{N,O,NO,O_2(^1\Delta_g)}, \tag{17}$$

where the A_i, B_i, C_i and E_i coefficients are given by

$$A_i = D_i + K, \tag{18}$$

$$B_i = \frac{\partial (D_i + K)}{\partial z} + (D_i + K)\frac{\partial (\ln T)}{\partial z} + \left(\frac{D_i}{H_i} + \frac{K}{H}\right), \tag{19}$$

$$C_i = -u, \tag{20}$$

$$E_i = (D_i + K)\frac{\partial^2 (\ln T)}{\partial z^2} + \frac{\partial (D_i + K)}{\partial z}\frac{\partial (\ln T)}{\partial z} + \frac{1}{H_i}\frac{\partial D_i}{\partial z} + \frac{1}{H}\frac{\partial K}{\partial z} - \frac{D_i}{H_i^2}\frac{\partial H_i}{\partial z} - \frac{K}{H^2}\frac{\partial H}{\partial z}. \tag{21}$$

The problem can also be cast using a matrix form such as

$$\frac{\partial \vec{n}}{\partial t} = \mathbf{A}\frac{\partial^2 \vec{n}}{\partial z^2} + \mathbf{B}\frac{\partial \vec{n}}{\partial z} + \mathbf{C}\frac{\partial \vec{n}}{\partial x} + \mathbf{E}\vec{n} + \vec{f}(\vec{n}), \tag{22}$$

where **A**, **B**, **C** and **E** are diagonal matrixes and $\vec{f}(\vec{n})$ takes into account the chemical kinetics of the problem. In fact, it is this only term that introduces a nonlinearity into the problem and induces coupling between the four partial differential equations. The $\vec{n}$ vector in Eq. (22) represents the number densities of the four minor species, namely $\vec{n} = (n_{\mathrm{N}}, n_{\mathrm{O}}, n_{\mathrm{NO}}, n_{\mathrm{O_2(^1\Delta_g)}})^T$. The $\vec{f}(\vec{n})$ vector can be written in an explicit way:

$$\begin{pmatrix} f_{\mathrm{N}} \\ f_{\mathrm{O}} \\ f_{\mathrm{NO}} \\ f_{\mathrm{O_2(^1\Delta_g)}} \end{pmatrix} = \begin{pmatrix} -k_1 n_{\mathrm{N}} n_{\mathrm{O}} - k_2 n_{\mathrm{N}} n_{\mathrm{O}} n_{\mathrm{CO2}} - k_3 n_{\mathrm{N}} n_{\mathrm{NO}} \\ k_3 n_{\mathrm{N}} n_{\mathrm{NO}} - k_1 n_{\mathrm{N}} n_{\mathrm{O}} - k_2 n_{\mathrm{N}} n_{\mathrm{O}} n_{\mathrm{CO2}} - k_4 n_{\mathrm{O}}^2 n_{\mathrm{CO2}} \\ k_1 n_{\mathrm{N}} n_{\mathrm{O}} + k_2 n_{\mathrm{N}} n_{\mathrm{O}} n_{\mathrm{CO2}} - k_3 n_{\mathrm{N}} n_{\mathrm{NO}} \\ (\varepsilon k_4) n_{\mathrm{O}}^2 n_{\mathrm{CO2}} - k_5 n_{\mathrm{O_2(^1\Delta_g)}} n_{\mathrm{CO2}} - k_6 n_{\mathrm{O_2(^1\Delta_g)}} \end{pmatrix}, \tag{23}$$

where ε is the efficiency of the production of $\mathrm{O_2(^1\Delta_g)}$ in reaction (14). In this study, we use an efficiency value $\varepsilon = 0.75$ suggested by Crisp et al. (1996) on the basis of the constraints derived from $\mathrm{O_2}$ infrared Earth airglow.

2.2. Characteristic times of the relative processes

In order to estimate the role of dynamics and chemical kinetics, the characteristic times of the different phenomena taken into account in the model have been examined. First, we determine the species lifetimes relative to each chemical reaction. In order to estimate the different e-folding lifetimes of the processes, the vertical profiles of the number densities of the four minor species are required. They are taken from the one-dimensional diffusion-reaction model described by Gérard et al. (2008a). In addition, we can examine the overall chemical lifetime τ_A of each minor species which is given by

$$\tau_A = \frac{1}{\frac{1}{\tau_{A_1}} + \frac{1}{\tau_{A_2}} + \cdots + \frac{1}{\tau_{A_n}}}, \tag{24}$$

where τ_A is the overall chemical lifetime of species A, and $\tau_{A_1}, \ldots, \tau_{A_n}$ are the lifetimes of A due to loss from reactions $1,\ldots,n$, respectively. We now examine the characteristic times of the transport processes. Given that the vertical molecular diffusive flux of a minor constituent i (8) is known, we can directly get the vertical molecular diffusive velocity for constituent $v^i_{mol.diff.}$ (i.e. $(\Phi^i_{mol.diff.})_z = n_i \times v^i_{mol.diff.}$). Indeed, the characteristic time for molecular diffusion of the species i is given by $\tau^i_{mol.diff.} \approx H_i^2/D_i$. To estimate the characteristic time of the eddy diffusion $\tau^i_{edd.diff.}$, the characteristic length is the atmosphere scale height and it follows that $\tau^i_{edd.diff.} \approx H^2/K$. These different characteristic times are represented in Fig. 1.

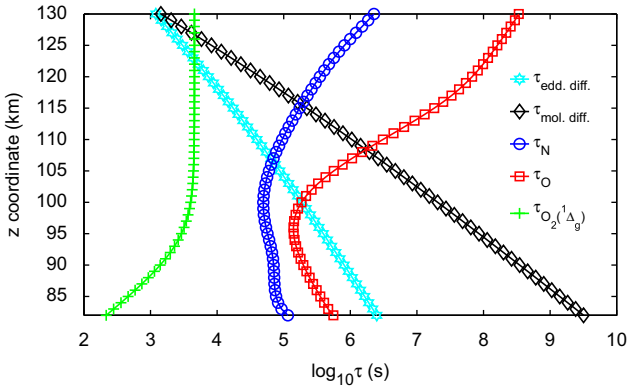

Fig. 1. Overall chemical lifetime of N, O and $\mathrm{O_2(^1\Delta_g)}$ and characteristic times of the vertical transport processes taken in account in the model. The molecular diffusion coefficient of N has been used to compute the characteristic time of the molecular diffusion.

In Fig. 1, it can be observed that there are many different time scales in this study. First, we focus on the overall chemical lifetimes of N, O and $\mathrm{O_2(^1\Delta_g)}$. The overall chemical lifetime of atomic oxygen is by far the longest in comparison with the other two, especially at the higher altitudes.[1] Consequently, atomic oxygen will be more subject to transport inside the solving domain than N and $\mathrm{O_2(^1\Delta_g)}$. Comparing transport lifetimes, Fig. 1 shows that eddy diffusion is the dominant process up to approximately $z = 130$ km. For higher altitudes, the molecular diffusion dominates over eddy diffusion, as expected from the altitude of the turbopause, experimentally determined by von Zahn et al. (1979).

2.3. Numerical method

In order to solve system (22), made of four nonlinear coupled partial differential equations, we use a cell-centered finite volume method. This method uses the integral form of the balance equations as a starting point. Consequently, we have to transform the local form of the continuity equation (7) into its integral form. Considering an arbitrary fixed surface $\mathcal{S}$ (Eulerian approach), it just has to integrate the Eq. (7) on this surface $\mathcal{S}$ (volume control in two spatial dimensions):

$$\frac{d}{dt}\int_{\mathcal{S}} n_i d\mathcal{S} + \int_{\mathcal{S}} \frac{\partial (\Phi^i_{adv})_x}{\partial x} d\mathcal{S} + \int_{\mathcal{S}} \frac{\partial (\Phi^i_{diff})_z}{\partial z} d\mathcal{S} = \int_{\mathcal{S}} (P_i - L_i)\, d\mathcal{S}. \tag{25}$$

Using the divergence theorem, Eq. (25) may be written as

$$\frac{d}{dt}\int_{\mathcal{S}} n_i\, d\mathcal{S} + \oint_{\mathcal{C}} (\Phi^i_{adv})_x n_x\, d\mathcal{C} + \oint_{\mathcal{C}} (\Phi^i_{diff})_z n_z\, d\mathcal{S} = \int_{\mathcal{S}} (P_i - L_i)\, d\mathcal{S}, \tag{26}$$

where $\mathcal{C}$ is the contour line holding the surface $\mathcal{S}$, n_x and n_z are the Cartesian components of the outward unit vector normal to the surface $\mathcal{S}$.

2.3.1. Spatial discretization

In order to discretize the two-dimensional problem, we have divided the solving domain into a set of rectangular cells (control volumes).

[1] Rigorously, the z coordinate is not the altitude of the Venus atmosphere. Nevertheless, from now on, we call it altitude.

The independent variables x and z are discretized such as

$$x_m = (m-\tfrac{1}{2})\Delta x \quad \forall m \in [\tfrac{1}{2},1,\ldots,M,M+\tfrac{1}{2}], \tag{27}$$

$$z_n = (n-\tfrac{1}{2})\Delta z \quad \forall n \in [\tfrac{1}{2},1,\ldots,N,N+\tfrac{1}{2}], \tag{28}$$

where Δx and Δz are, respectively, the spatial steps in the horizontal and vertical directions. Therefore, the solving domain is covered with $(M \times N)$ rectangular cells. Moreover, the spatial steps in the two directions have been chosen to be constant in the whole domain and such as $\Delta x \neq \Delta z$. Practically, we have taken $\Delta x = 100$ km and $\Delta z = 1$ km for all simulations described in Section 3.

Now, let us consider the cell control labelled by indices m and n, whose the surface $\mathcal{S}$ is delimited by horizontal boundaries noted by indices $m-1/2$ and $m+1/2$, and by vertical boundaries noted by indices $n-1/2$ and $n+1/2$, as seen in Fig. 2. Consequently, Eq. (26) can be cast:

$$\begin{aligned}\int_{z_{n-1/2}}^{z_{n+1/2}}\int_{x_{m-1/2}}^{x_{m+1/2}}(P_i-L_i)\,dx\,dz &= \frac{d}{dt}\int_{z_{n-1/2}}^{z_{n+1/2}}\int_{x_{m-1/2}}^{x_{m+1/2}} n_i\,dx\,dz \\ &+ \int_{z_{n-1/2}}^{z_{n+1/2}}[(\Phi^i_{adv})_x|_{m+1/2,n}-(\Phi^i_{adv})_x|_{m-1/2,n}]\,dz \\ &+ \int_{x_{m-1/2}}^{x_{m+1/2}}[(\Phi^i_{diff})_z|_{m,n+1/2}-(\Phi^i_{diff})_z|_{m,n-1/2}]\,dx.\end{aligned} \tag{29}$$

After a few mathematical manipulations, it can be shown that:

$$\begin{aligned}&\int_{z_{n-1/2}}^{z_{n+1/2}}[(\Phi^i_{adv})_x|_{m+1/2,n}-(\Phi^i_{adv})_x|_{m-1/2,n}]\,dz \\ &= \Delta z[(\Phi^i_{adv})_x|_{m+1/2,n}-(\Phi^i_{adv})_x|_{m-1/2,n}]+\mathcal{O}(\Delta z^3\Delta x),\end{aligned} \tag{30}$$

$$\begin{aligned}&\int_{x_{m-1/2}}^{x_{m+1/2}}[(\Phi^i_{diff})_z|_{m,n+1/2}-(\Phi^i_{diff})_z|_{m,n-1/2}]\,dz \\ &= \Delta x[(\Phi^i_{diff})_z|_{m,n+1/2}-(\Phi^i_{diff})_z|_{m,n-1/2}]+\mathcal{O}(\Delta x^3\Delta z).\end{aligned} \tag{31}$$

Moreover, defining the cell-average number density $\overline{n}_i$, the cell-average chemical production rate $\overline{P}_i$ and the cell-average chemical loss rate $\overline{L}_i$ of the minor species i for cell (m,n):

$$(\overline{n}_i)_{m,n} = \frac{1}{\Delta x\Delta z}\int_{z_{n-1/2}}^{z_{n+1/2}}\int_{x_{m-1/2}}^{x_{m+1/2}} n_i\,dx\,dz, \tag{32}$$

$$(\overline{P}_i)_{m,n} = \frac{1}{\Delta x\Delta z}\int_{z_{n-1/2}}^{z_{n+1/2}}\int_{x_{m-1/2}}^{x_{m+1/2}} P_i\,dx\,dz, \tag{33}$$

$$(\overline{L}_i)_{m,n} = \frac{1}{\Delta x\Delta z}\int_{z_{n-1/2}}^{z_{n+1/2}}\int_{x_{m-1/2}}^{x_{m+1/2}} L_i\,dxdz, \tag{34}$$

and inserting (30), (31), (32), (33) and (34) in Eq. (29), it follows that:

$$\begin{aligned}(\overline{P}_i)_{m,n}-(\overline{L}_i)_{m,n} &= \frac{d}{dt}(\overline{n}_i)_{m,n}+\frac{[(\Phi^i_{adv})_x|_{m+1/2,n}-(\Phi^i_{adv})_x|_{m-1/2,n}]}{\Delta x}+\mathcal{O}(\Delta z^2) \\ &+\frac{[(\Phi^i_{diff})_z|_{m,n+1/2}-(\Phi^i_{diff})_z|_{m,n-1/2}]}{\Delta z}+\mathcal{O}(\Delta x^2).\end{aligned} \tag{35}$$

In addition, it can be shown that:

$$(\overline{n}_i)_{m,n} = (n_i)_{m,n}+\mathcal{O}(\Delta x^2)+\mathcal{O}(\Delta z^2), \tag{36}$$

$$(\overline{P}_i)_{m,n} = (P_i)_{m,n}+\mathcal{O}(\Delta x^2)+\mathcal{O}(\Delta z^2), \tag{37}$$

$$(\overline{L}_i)_{m,n} = (L_i)_{m,n}+\mathcal{O}(\Delta x^2)+\mathcal{O}(\Delta z^2). \tag{38}$$

Furthermore, given (36), (37) and (38), a second-order accurate approximation in Δx and Δz is obtained when the cell-average of n_i, P_i and L_i are approximated by their values at computational nodes (center of the cells):

$$(\overline{n}_i)_{m,n} \approx (\tilde{\overline{n}}_i)_{m,n} = (n_i)_{m,n}, \tag{39}$$

$$(\overline{P}_i)_{m,n} \approx (\tilde{\overline{P}}_i)_{m,n} = (P_i)_{m,n}, \tag{40}$$

$$(\overline{L}_i)_{m,n} \approx (\tilde{\overline{L}}_i)_{m,n} = (L_i)_{m,n}. \tag{41}$$

Note that we have used the tilde symbol ˜ to differentiate exact and approximated values. In the rest of this study, all physical quantities noted with the tilde symbol are approximated values.

In addition, it can be seen in Eq. (35) that both fluxes (diffusive and advective) are required at cell faces, not at computational nodes. Consequently, we need to approximate the face values of fluxes in terms of the values at computational nodes. Physically, it is important to note that diffusive and advective processes are very different. The main difference between these two processes, from a numerical point of view, is that the advective process is a directional process while the diffusive process is not. Indeed, the advective process transports properties only in the direction of the flow. In order to take the physical nature of these two processes into account, we have used central differencing for diffusive flux and upwind scheme for advective flux (Hundsdorfer and Verwer, 2007; Karniadakis and Kirby, 2005). First, we consider the (horizontal) advective flux (Fig. 3).

In upwind scheme, $(\Phi^i_{adv})_x|_{m+1/2,n}$ is taken as the value at the upwind computational node. Namely, it follows that:

$$\begin{aligned}(\Phi^i_{adv})_x|_{m+1/2,n} &\approx (\tilde{\Phi}^i_{adv})_x|_{m+1/2,n} \\ &= \begin{cases}(\Phi^i_{adv})_x|_{m,n} = u_{m+1/2,n}(n_i)_{m,n} & \text{if } u_{m+1/2,n} > 0, \\ (\Phi^i_{adv})_x|_{m+1,n} = u_{m+1/2,n}(n_i)_{m+1,n} & \text{if } u_{m+1/2,n} < 0.\end{cases}\end{aligned} \tag{42}$$

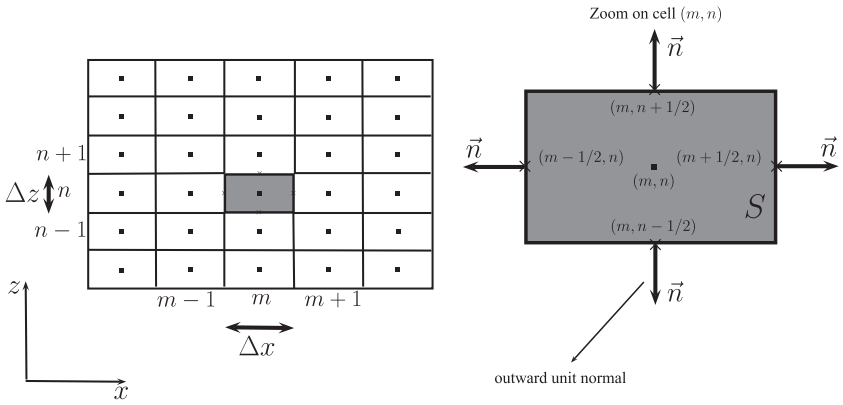

Fig. 2. Staggered-grid covering the whole solving domain.

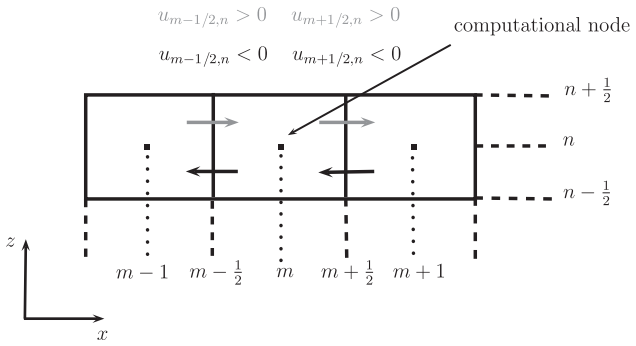

Fig. 3. Upwind scheme for advective process.

As for $(\Phi^i_{adv})_x|_{m-1/2,n}$, using the same procedure, it follows that:

$$(\Phi^i_{adv})_x|_{m-1/2,n} \approx (\tilde{\Phi}^i_{adv})_x|_{m-1/2,n} = \begin{cases} (\Phi^i_{adv})_x|_{m-1,n} = u_{m-1/2,n}(n_i)_{m-1,n} & \text{if } u_{m-1/2,n} > 0, \\ (\Phi^i_{adv})_x|_{m,n} = u_{m-1/2,n}(n_i)_{m,n} & \text{if } u_{m-1/2,n} < 0. \end{cases} \quad (43)$$

Further, given that the horizontal component u of the velocity field $\vec{v}$ does not change with the x coordinate (by hypothesis) and working with a regular mesh, it can be shown that this reconstruction method is a first-order accurate approximation in Δx.

Now, we focus on the diffusive flux. Considering Eq. (8), we can see that diffusive flux can be cast such as

$$(\Phi^i_{diff})_z = -\alpha \frac{\partial n_i}{\partial z} - \beta n_i, \quad (44)$$

assuming that:

$$\alpha = (D_i + K), \quad (45)$$

$$\beta = (D_i + K)(1/T)(\partial T/\partial z) + (D_i/H_i) + (K/H). \quad (46)$$

In order to reconstruct the values of this flux at cell faces, a central differencing method has been used to discretize the first spatial derivative because diffusion is not a directional process unlikely to advection. As for the second term in the right-hand-side of the Eq. (44), we use a central weighting between the two directly adjacent computational nodes to the considered cell face. Therefore, the diffusive fluxes $(\Phi^i_{diff})_z|_{m,n+1/2}$ and $(\Phi^i_{diff})_z|_{m,n-1/2}$ are approximated such as

$$(\Phi^i_{diff})_z|_{m,n+1/2} \approx (\tilde{\Phi}^i_{diff})_z|_{m,n+1/2} \approx -\alpha_{m,n+1/2} \frac{(n_i)_{m,n+1} - (n_i)_{m,n}}{\Delta z} - \beta_{m,n+1/2} \frac{(n_i)_{m,n} + (n_i)_{m,n+1}}{2}, \quad (47)$$

$$(\Phi^i_{diff})_z|_{m,n-1/2} \approx (\tilde{\Phi}^i_{diff})_z|_{m,n-1/2} \approx -\alpha_{m,n-1/2} \frac{(n_i)_{m,n} - (n_i)_{m,n-1}}{\Delta z} - \beta_{m,n-1/2} \frac{(n_i)_{m,n} + (n_i)_{m,n-1}}{2}. \quad (48)$$

Given that α and β are continuous with the z coordinate and working with a regular mesh, it can be shown that this discretization is a second-order accurate approximation in Δz.

In addition, inserting the different approximated physical quantities given by (39)–(43), (47) and (48) in Eq. (35), we can see that the adopted spatial numerical scheme is a second-order accurate approximation in Δz and a first-order accurate approximation in Δx. Therefore, this spatial numerical scheme is globally a first-order accurate approximation.

Moreover, in order to help further modelling works, the location storage of each physical quantity at play in the model is given in Table 2.

Table 2
Storage location of the different physical quantities for cell (m, n).

Storage location	Physical quantity
$(m \pm 1/2, n)$	u
$(m, n \pm 1/2)$	T, K, H, H_i, D_i
(m,n)	n_i, P_i, L_i, k_1, k_2, k_3, k_4, k_5, k_6

All of these physical quantities have been defined previously in this study.

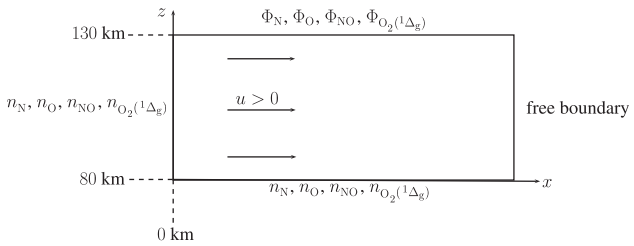

Fig. 4. Solving domain and conditions imposed at the boundaries of the solving domain.

2.3.2. Temporal discretization

With regard to the temporal discretization, a forward Euler scheme (Hundsdorfer and Verwer, 2007; Jacobson, 2005; Karniadakis and Kirby, 2005) has been used. The time step Δt used in the model is fixed and does not change with the number of temporal iterations. Concretely, we have used a time step Δt equal to 20 s for all simulations described in Section 3. Moreover, this numerical scheme is a first-order accurate approximation in Δt. Given that an explicit scheme has been used, a stability condition has to be satisfied for each temporal iteration. Indeed, the time step cannot be taken in a arbitrary way. Its maximum value depends on the values used for the spatial steps Δx and Δz. In spite of this constraint, an explicit scheme rather than a semi-implicit has been adopted, which offers the possibility to be unconditionally stable, for several arguments. First, the main purpose of this numerical model is to investigate the spatio-temporal behavior of the minor species. Consequently, we have to choose time steps which are not too large in order to be able to detect the small temporal variations of the problem. Therefore, the main interest of semi-implicit schemes is not used if small time steps are used. Second, the computational cost for one temporal iteration is much larger for a semi-implicit scheme than for an explicit one.

2.4. Boundary and initial conditions

A flux condition is applied through the upper boundary and photochemical equilibrium at the lower boundary is assumed as shown in Fig. 4. Moreover, in order to adjust the peak altitudes of the volume emission rates of the $O_2(^1\Delta_g)$ infrared and NO ultraviolet nightglows, a sensibility study of the model has been carried out, neglecting the horizontal direction and considering the steady state solution. Under these conditions, our model is reduced to a one-dimensional time-independent model. Based on this study, we adopt the following parameter values: $A = 2 \times 10^{13}$, $\Phi_N^{Constant} = 10^{10}\,cm^{-2}\,s^{-1}$ and $\Phi_O^{Constant} = 2 \times 10^{12}\,cm^{-2}\,s^{-1}$. With these values, the altitudes of the peak volume emission

rates of the NO ultraviolet and $O_2(^1\Delta_g)$ infrared nightglows are located, respectively, at 110.5 and 101.5 km. Observations show that the altitudes of the peak volume emission rates of these two nightglows are typically located near 115 and 100 km, respectively, for the NO ultraviolet and $O_2(^1\Delta_g)$ infrared nightglows, respectively. In addition, as seen in Fig. 4, the direction of the fluid is from the left to the right of the domain (i.e. $u>0$). Consequently, we impose boundary conditions only on the left boundary and the right boundary is free. The left boundary conditions are taken as the vertical stationary profiles of the four number densities obtained from the one-dimensional steady state solutions, using the parameter values mentioned previously. Furthermore, a priori, the distance at which the right boundary is located is not fixed in the model. Indeed, this distance will have to be taken such as the influence of horizontal transport on the spatial distribution of number densities can be observed. The right-side boundary has been fixed at $x=8900$ km. The horizontal wind velocity at the level of the O_2 airglow layer is very variable as was recently summarized by Lellouch et al. (2008). Winds velocities, derived from CO millimeter observations, are typically on the order of 30–50 m s^{-1} at $\sim$93 km and 90–120 m s^{-1} near 102 km. Hueso et al. (2008) derived values of the effective wind velocity at 97 km of a few tens of m s^{-1} from the motions of bright spots of O_2 airglow. Horizontal winds calculated with the VTGCM (Bougher et al., 1990) values are on the same order in the region separating the two emission layers. Therefore, we adopt a value of 25 m s^{-1} for the horizontal component u of the velocity field for all simulations described in this study. This value represents a reasonable average of dynamical observations and modelling results. The values used for the different boundary conditions are summarized in Tables 3 and 4.

Table 3
Upper and lower boundary conditions.

Constituent	Upper boundary (cm^{-2} s^{-1})	Lower boundary (cm^{-3})
N	$\Phi_N=\Phi_N^{Constant}$ or $\Phi_N(x)$, given by (49)	$n_N=100$
O	$\Phi_O=\Phi_O^{Constant}$ or $\Phi_O(x)$, given by (50)	$n_O=100$
NO	$\Phi_{NO}=0$	$n_{NO}=100$
$O_2(^1\Delta_g)$	$\Phi_{O_2(^1\Delta_g)}=0$	$n_{O_2(^1\Delta_g)}=100$

Table 4
Left boundary conditions.

Constituent	Left boundary (cm^{-3})	Right boundary
N	$n_N=n_N^\star(z)$	No constraint
O	$n_O=n_O^\star(z)$	No constraint
NO	$n_{NO}=n_{NO}^\star(z)$	No constraint
$O_2(^1\Delta_g)$	$n_{O_2(^1\Delta_g)}=n^\star_{O_2(^1\Delta_g)}(z)$	No constraint

The $\star$ symbol means that it is the number density profiles taken from the one-dimensional steady state model with $A=2\times10^{13}$, $\Phi_N^{Constant}=10^{10}$ cm^{-2} s^{-1} and $\Phi_O^{Constant}=2\times10^{12}$ cm^{-2} s^{-1}.

3. Simulations and discussion of the results

3.1. Two-dimensional steady state solutions

In order to simulate inhomogeneities of the spatial distribution of the $O_2(^1\Delta_g)$ infrared nightglow (Hueso et al., 2008) and the NO ultraviolet nightglow (Stewart et al., 1980), the downward flux of O and N atoms imposed at the upper boundary have been taken nonhomogeneous along the x coordinate. Consequently, the downward flux of O and N atoms through the upper boundary is no longer fixed to a constant value as in the one-dimensional model. To achieve this goal, downward fluxes such as these seen in Fig. 5 have been adopted. These consist of a superposition of a constant flux imposed at the whole upper boundary and a Gaussian-shaped flux which is such as the peak of the Gaussian function is centered on $x=2000$ km and the full width at half maximum of the peak of the Gaussian function is equal to 1000 km, which approximately corresponds to the typical size of enhanced regions of O_2 infrared nightglow (Allen et al., 1992; Crisp et al., 1996; Lellouch et al., 1997). As a result, the maximum value of both fluxes are increased by a factor of 10 at $x=2000$ km in comparison with the constant fluxes applied through the entire upper boundary. Mathematically, fluxes of O and N atoms applied through the upper boundary can be written as functions of the x coordinate such as

$$\Phi_N(x)=\Phi_N^{Constant}+9\times\Phi_N^{Constant}\times G(x), \quad (49)$$

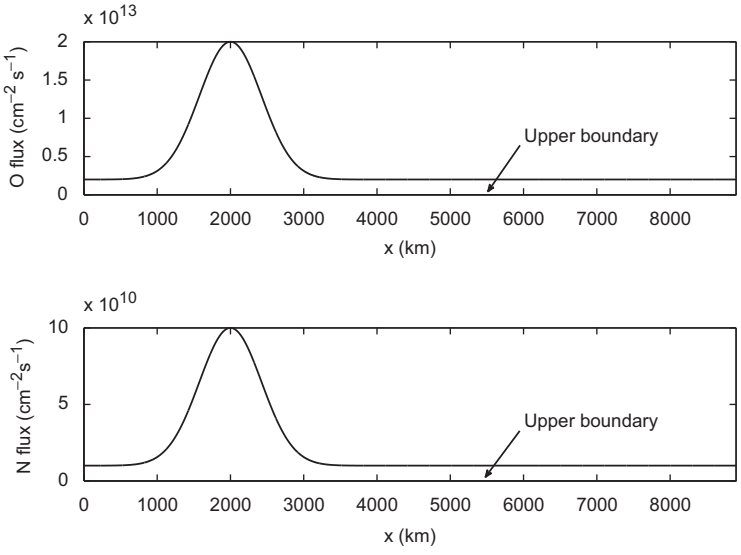

Fig. 5. Downward flux of O and N atoms, respectively, given by (50) and (49), through the upper boundary of the solving domain resulting of the superposition of a constant flux and a Gaussian-shaped flux.

$$\Phi_O(x) = \Phi_O^{Constant} + 9 \times \Phi_O^{Constant} \times G(x), \quad (50)$$

where $G(x)$ is a normalized Gaussian function whose features have just been mentioned previously.

Fig. 6 shows the results of this steady state simulation for the N (Fig. 6a) and O (Fig. 6b) density fields, respectively. We first note that the peaks of the N and O number densities are separated by ~ 10 km following the altitude. Moreover, these two plates also show a significant difference relative to the horizontal position of these two peaks. Indeed, the maximum density of N is located approximately 450 km downwind from the center of the region of enhanced supply of N and O while the O maximum density is approximately 2250 km away from this region. Consequently, as suggested by the discussion of the chemical lifetimes, it clearly appears that atomic oxygen is more subject to transport than atomic nitrogen. Indeed, as was shown in Fig. 1, at 130 km, the chemical lifetime of atomic oxygen is approximately 100 times longer than that of atomic nitrogen. Therefore, it is obvious that nitrogen atoms will be chemically consumed by reaction (13) faster than oxygen atoms. We now compare the volume emission rates of the NO and $O_2(^1\Delta_g)$ nightglows. First, Fig. 6c shows that the peak volume emission rate of NO is roughly equal to 2.7×10^4 photons $cm^{-3}\,s^{-1}$, that is, the peak value is approximately multiplied by a factor of 7.5 when the enhanced supply of N and O atoms is applied in comparison with a constant supply of O and N atoms, as indicated in Tables 5 and 6. Moreover, it can be seen that the peak altitude has significantly increased, moving from 110.5 to 116.5 km. We also note that the spatial distribution of the volume emission rate is very similar to the number density of N. This feature confirms the analysis carried out by Stewart et al. (1980) which indicated that the spatial distribution of the ultraviolet nightglow of NO reflects that of the atomic nitrogen flux applied through the upper boundary. Fig. 6d shows that the peak volume emission rate of the infrared nightglow is located

Table 5
Location and volume emission rate (V.E.R.) of the peak of the $O_2(^1\Delta_g)$ infrared and NO ultraviolet nightglows with a constant supply of O and N atoms through the whole upper boundary.

	$V.E.R._{peak}$ (photons $cm^{-3}\,s^{-1}$)	z_{peak} (km)
$O_2(^1\Delta_g)$ nightglow	1.4×10^6	101.5
NO nightglow	3.6×10^3	110.5

Table 6
Location and volume emission rate (V.E.R.) of the peak of the $O_2(^1\Delta_g)$ infrared and NO ultraviolet nightglows with an enhanced supply of O and N atoms through a limited region of the upper boundary, as seen in Fig. 5, during all the simulation.

	$V.E.R._{peak}$ (photons $cm^{-3}\,s^{-1}$)	z_{peak} (km)	x_{peak} (km)
$O_2(^1\Delta_g)$ nightglow	3.5×10^6	103.5	5850
NO nightglow	2.7×10^4	116.5	2650

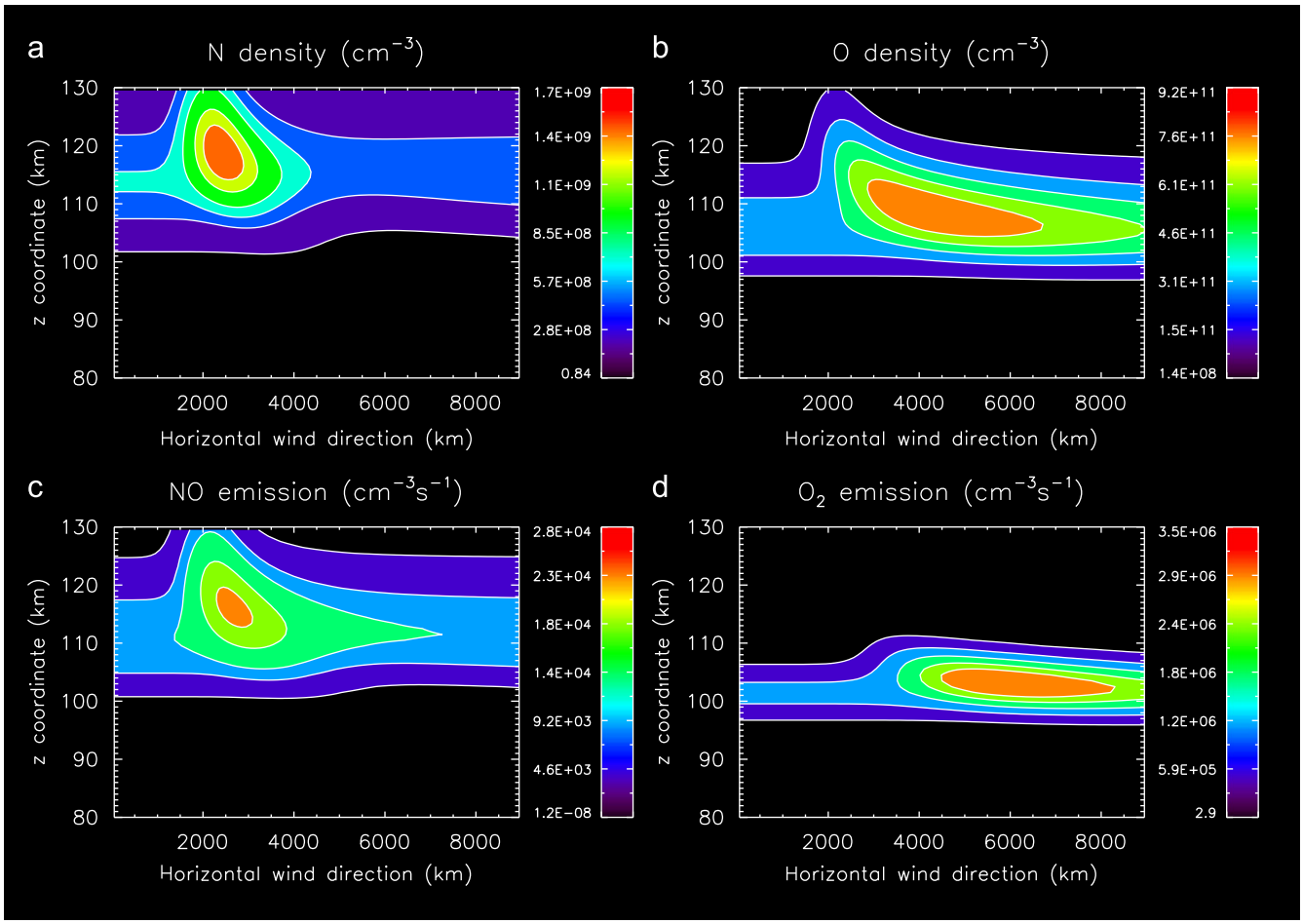

Fig. 6. Spatial distributions of the N (a) and O (b) number densities; spatial distributions of the volume emission rates of NO ultraviolet (c) and $O_2(^1\Delta_g)$ infrared (d) nightglows.

~ 3850 km from the center of the enhanced supply of atoms, that is 1600 km downwind from the peak density of atomic oxygen. Moreover, it can be seen that the position of the peak of the $O_2(^1\Delta_g)$ nightglow, is also shifted downward by 6 km in comparison with the maximum number density of O. This behavior can be explained by examining the production rate of the number density of the excited molecular oxygen in the $O_2(^1\Delta_g)$ singlet state which is the origin of the infrared nightglow. This production rate is given by $(\varepsilon k_4) \times n_O^2 \times n_{CO_2}$. So, this one depends on the number density of O and CO_2. In addition, as we already noted in Fig. 6b, the maximum density of O is located at ~ 108.5 km and then decreases as altitude decreases. Nevertheless, the profile of the number density of CO_2 continues to increase with decreasing altitude. Consequently, the $O_2(^1\Delta_g)$ maximum is located at a lower altitude than the one of O. Besides, it is interesting to emphasize that the peak volume emission rate of $O_2(^1\Delta_g)$ is increased by a factor of 2.6 approximately in comparison to the solution for a homogeneous downward flux of O and N atoms. Moreover, as seen in Fig. 6c and d, the peak volume emission rate of NO is located closer to center of the region of enhanced atom flux than the $O_2(^1\Delta_g)$ infrared nightglow. As a consequence, this feature indicates that the NO ultraviolet nightglow is a better diagnostic of regions where with an enhanced supply of atoms than the $O_2(^1\Delta_g)$ infrared nightglow.

3.2. Two-dimensional time-dependent solutions

In this section, we add the time dimension to the model described in Section 3.1, which is now time-dependent. In order to illustrate some results obtained from the time-dependent model, we focus on the spatio-temporal distribution of the NO ultraviolet nightglow. The boundary conditions, left and lower boundary conditions are unchanged in comparison to those applied in the

Table 7
Upper boundary conditions for the two-dimensional time-dependent simulation.

Time (h)	Φ_N(cm^{-2} s^{-1})	Φ_O (cm^{-2} s^{-1})	Φ_{NO} (cm^{-2} s^{-1})	$\Phi_{O_2(^1\Delta_g)}$ (cm^{-2} s^{-1})
$0 \le t \le \sim 8.33$	$\Phi_N(x)$	$\Phi_O(x)$	0	0
$t > \sim 8.33$	$\Phi_N^{Constant}$	$\Phi_O^{Constant}$	0	0

$\Phi_N(x)$ and $\Phi_O(x)$ are, respectively, given by (49) and (50).

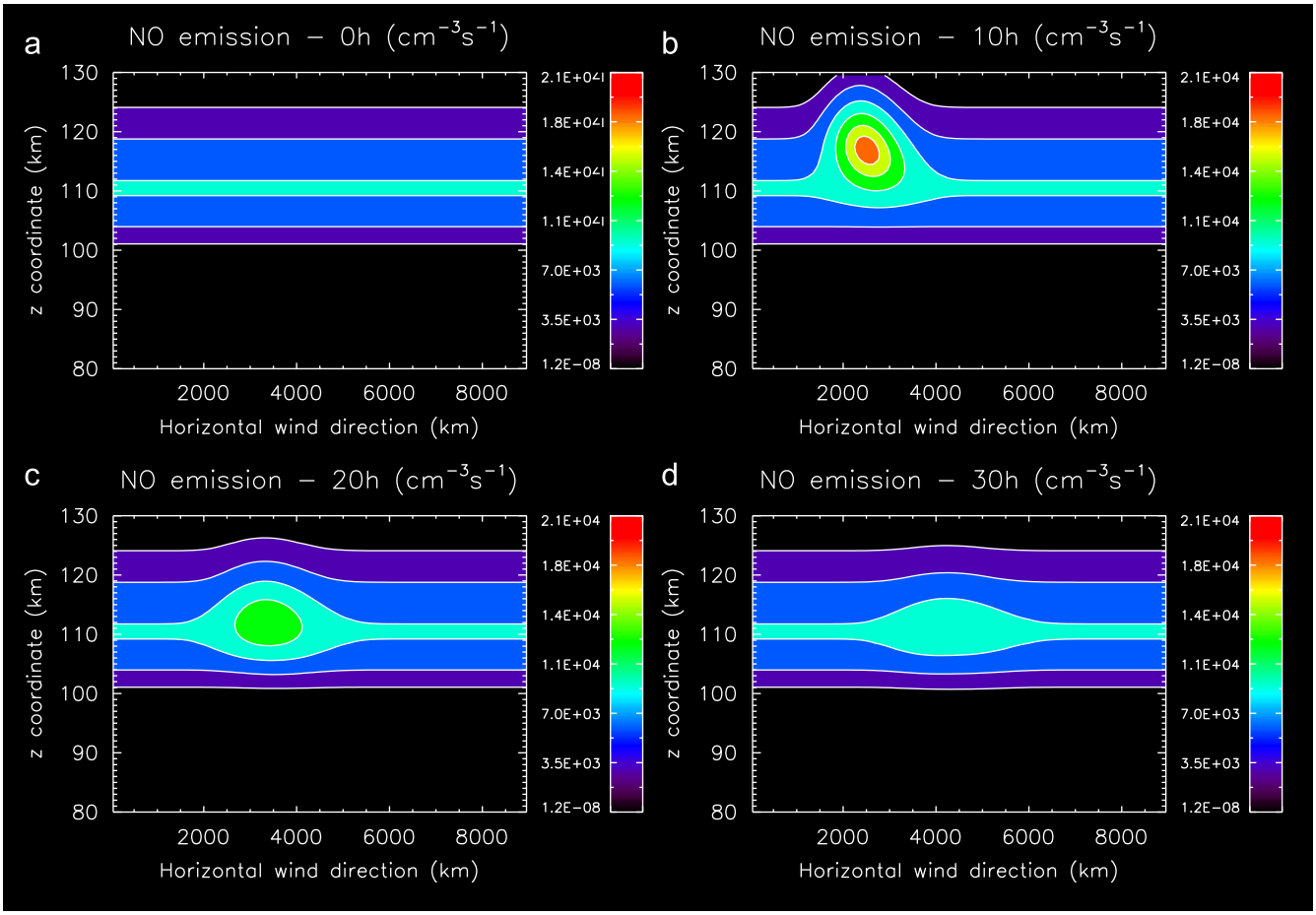

Fig. 7. Temporal evolution of spatial distribution of the volume emission rate of the NO ultraviolet nightglow: (a) initial state, which is homogeneous relative to the horizontal wind direction; (b) spatial distribution after 10 h of simulation; (c) spatial distribution after 20 h of simulation; and (d) spatial distribution after 30 h of simulation. The same color scale has been used for all snapshots.

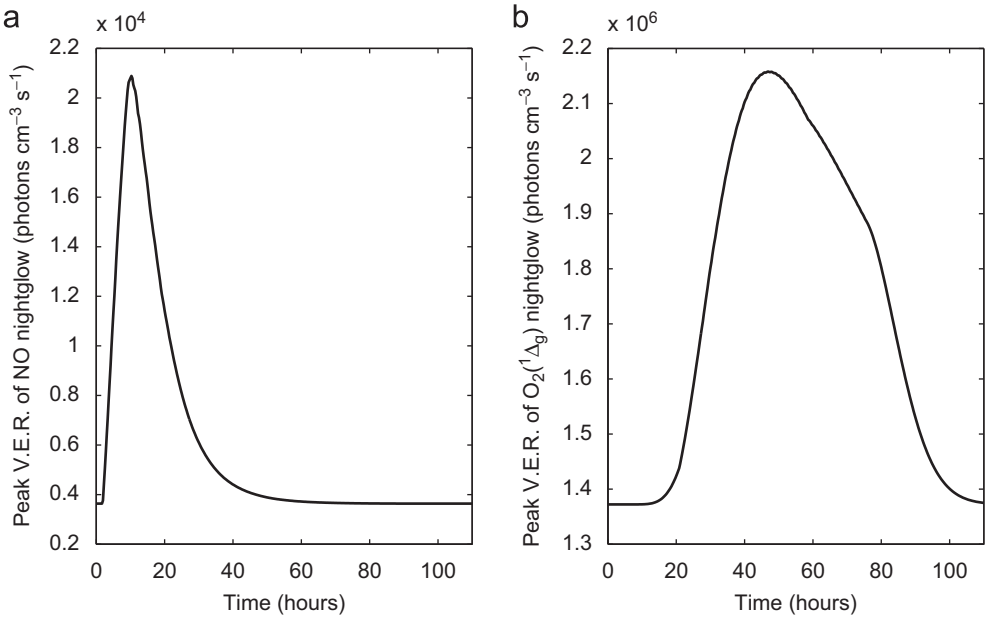

Fig. 8. Time evolution of the peak volume emission rate (V.E.R.) of the NO ultraviolet (a) and $O_2(^1\Delta_g)$ infrared (b) nightglows.

time-independent model. On the other hand, the upper boundary condition is now time-dependent in order to simulate temporal variations of both nightglows. They are summarized in Table 7.

As for the initial conditions, for each number density, we have imposed the spatial distribution obtained from the two-dimensional time-independent simulation with a constant atoms supply in the time through the upper boundary, which is homogeneous relative to the x coordinate. In fact, the enhanced supply of atoms during the given time interval specified in Table 7, generates a perturbation of this two-dimensional time-independent solution. Then, we let the system evolve until it returns to its initial stationary state, homogeneous relative to the x coordinate.

As seen in Figs. 7b and 8a, after 10 h of simulation, the influence of the enhanced atom supply is clearly visible. Indeed, the volume emission rate has already reached its maximum value, that is, $\sim 2.1\times10^4$ photons cm^{-3} s^{-1}. At the same time, the spatial distribution of the number density of N is very close to the one of the NO volume emission rate. This result corroborates the analysis carried out by Stewart et al. (1980) previously mentioned in this study. About 10 h later, that is, 20 h after the beginning of the simulation, it can be seen in Fig. 7c that the peak NO volume emission rate has already strongly decreased. This situation can be explained by the close link between the N number density and the NO volume emission rate. Indeed, this last one is given by the $k_1\times n_N\times n_O$ product. Given that the chemical lifetime of nitrogen atoms is on the order of one day at $z=111.5$ km, as was shown in Fig. 1, a large part of nitrogen atoms injected into the solving domain has already been consumed by oxygen atoms after 20 h of simulated time. Consequently, there is no longer a large amount of nitrogen atoms to produce the ultraviolet NO nightglow, what explains the strongly decrease of the peak volume emission rate of NO. Fig. 7d shows that the spatial distribution of the NO volume emission rate, after 30 h of simulation has almost already returned in its initial state, homogeneous relative to the x coordinate.

Now, we focus on the temporal behaviors of the peak volume emission rates of the two emissions. Let us call $\Delta_{PeakV.E.R.}$ the difference between the maximum and minimum values of the peak volume emission rates of the two nightglows, $\Delta t^+_{1/2}$ the time where the peak volume emission rates of the two emissions have reached 50% of their $\Delta_{PeakV.E.R.}$ and $\Delta t^-_{1/2}$ the time needed to the maximum values of the peak volume emission rates decrease of 50% of their $\Delta_{PeakV.E.R.}$.

Table 8
Temporal behavior of the peak volume emission rates for the NO and $O_2(^1\Delta_g)$ nightglows.

	$\Delta_{PeakV.E.R.}$ (photons cm^{-3} s^{-1})	$\Delta t^+_{1/2}$ (h)	$\Delta t^-_{1/2}$ (h)
NO nightglow	$\sim 1.7253\times10^4$	~ 5	~ 9
$O_2(^1\Delta_g)$ nightglow	$\sim 7.8583\times10^5$	~ 29	~ 34

Fig. 8a shows that NO ultraviolet nightglow reacts almost immediately to a enhanced atom supply unlike to the $O_2(^1\Delta_g)$ infrared nightglow, as seen in Fig. 8b. Indeed, the peak volume emission rate of NO emission strongly increases just following the beginning of the atom fluxes increase. As seen in Table 8, it has already increased by 50% of its $\Delta_{PeakV.E.R.}$ after ~ 5 h whereas the peak volume emission rate of O_2 emission is still unaffected. The peak volume emission rate of NO nightglow reaches its maximum value after only ~ 1.5 h following the end of the enhanced atom supply, that is, after ~ 10 h of simulation. At the same time, the $O_2(^1\Delta_g)$ nightglow has not yet increased by 50% of its $\Delta_{PeakV.E.R.}$, i.e. $\Delta t^+_{1/2}\approx 29$ h for the $O_2(^1\Delta_g)$ emission. These results underline the lack of time-correlation between the two nightglows. The same observation is made when we examine the decreasing phases of the curves in Fig. 8a and b.

4. Conclusions

The development of this two-dimensional time-dependent model, coupling chemical and transport processes, has been essentially motivated by qualitative explanations proposed for the lack of correlation between the spatio-temporal behaviors of NO and $O_2(^1\Delta_g)$ nightglows. The steady state simulation, described in Section 3.1, has confirmed what Gérard et al. (2009) had shown from data obtained by VIRTIS and SPICAV instruments. Indeed, the peak volume emission rates of NO and $O_2(^1\Delta_g)$ nightglows are strongly spatially decorrelated, as was seen in Fig. 6c and d. The

two peaks are separated by a horizontal distance of $\sim$3200 km, corresponding to $\sim$2 h in terms of hour angle at the equator of Venus and by a vertical distance of $\sim$13 km, in approximate agreement with the $\sim$15 km observed mean gap in the statistical study carried out by Gérard et al. (2009). As qualitatively suggested by Gérard et al. (2009), the low degree of correlation between the NO and $O_2(^1\Delta_g)$ nightglows are due to the coupling between horizontal and vertical transport processes. Obviously, given that the chemical lifetimes of N and O atoms are very different and are governed by nonlinear processes, a two-dimensional numerical model was needed in order to confirm this suggestion and quantify the relative importance of different processes occurring in the Venus upper atmosphere. In addition, this steady state solution has also corroborated the analysis carried out by Stewart et al. (1980), indicating that the spatial distribution of the NO ultraviolet nightglow reflects rather well that of the atomic nitrogen supply through the upper boundary.

This steady state simulation has also emphasized that the NO ultraviolet nightglow is a better diagnostic of spatial inhomogeneities relative to the downward flowing atoms on the night side of Venus than the $O_2(^1\Delta_g)$ infrared nightglow. Moreover, in order to simulate localized enhancements of the atom supply, suggested by the presence of bright spots, a time dependence has been adopted for O and N fluxes through the upper boundary. Indeed, Stewart et al. (1980) and Hueso et al. (2008) have also shown large temporal variations of NO ultraviolet and $O_2(^1\Delta_g)$ infrared nightglows, respectively. This new dimension added to our numerical model has effectively shown that NO and $O_2(^1\Delta_g)$ nightglows are strongly time-decorrelated. The peak volume emission rate of NO nightglow is observed $\sim$10 h after the beginning of the enhanced supply of N and O whereas this one of $O_2(^1\Delta_g)$ nightglow is only observed after $\sim$48 h, that is, there is a time-shift of $\sim$38 h. Therefore, the NO ultraviolet nightglow is a better diagnostic for the temporal behavior of the downward flowing atoms than the $O_2(^1\Delta_g)$ infrared nightglow. Furthermore, when we compare the time-dependent simulation with the steady state results, we observe that peak volume emission rates for the two emissions are higher when the enhanced supply of atoms is applied during all the simulation. This result was expected given that volume emission rates increase with the enhancement of N and O. In addition, we have also noted that the NO and $O_2(^1\Delta_g)$ nightglows reach their peak values at higher or equal altitudes and located closer to center of the region of enhanced atom flux for the steady state simulation than for the time-dependent one. Finally, even though this numerical model is not a realistic description of the atmosphere of Venus, it has underlined the lack of spatio-temporal correlations between NO and $O_2(^1\Delta_g)$ nightglows in the presence of horizontal winds and has especially quantified the role of each process generating spatio-temporal de-correlations.

References

Allen, D., Crisp, D., Meadows, V., 1992. Variable oxygen airglow on Venus as a probe of atmospheric dynamics. Nature 359, 516–519.

Bailey, J., Meadows, V.S., Chamberlain, S., Crisp, D., 2008. The temperature of the Venus mesosphere from O2($a^1\Delta_g$) airglow observations. Icarus 197, 247–259.

Banks, P.M., Kockarts, G., 1973. Aeronomy, Part B. Elsevier, New York.

Bertaux, J.L., Nevejans, D., Korablev, O., Villard, E., Quémerais, E., Neefs, E., Montmessin, F., Leblanc, F., Dubois, J.P., Dimarellis, E., Hauchecorne, A., Lefèvre, F., Rannou, P., Chaufray, J.Y., Cabane, M., Cernogora, G., Souchon, G., Semelin, F., Reberac, A., Van Ransbeek, E., Berkenbosch, S., Clairquin, R., Muller, C., Forget, F., Hourdin, F., Talagrand, O., Rodin, A., Fedorova, A., Stepanov, A., Vinogradov, I., Kiselev, A., Kalinnikov, Y., Durry, G., Sandel, B., Stern, A., Gérard, J.C., 2007. SPICAV on Venus Express: three spectrometers to study the global structure and composition of the Venus atmosphere. Planet. Space Sci. 55, 1673–1700.

Bougher, S.W., Gérard, J.C., Stewart, A.I.F., Fesen, C.G., 1990. The Venus nitric oxide night airglow: model calculations based on the Venus thermospheric general circulation model. J. Geophys. Res. 95, 6271–6284.

Bougher, S.W., Rafkin, S., Drossart, P., 2006. Dynamics of the Venus upper atmosphere: outstanding problems and new constraints expected from Venus Express. Planet. Space Sci. 54, 1371–1380.

Campbell, I.M., Gray, C.N., 1973. Rate constants for O(^{3}P) recombination and association with N(^{4}S). Chem. Phys. Lett. 18, 607–609.

Campbell, I.M., Thrush, B.A., 1966. Behaviour of carbon dioxide and nitrous oxide in active nitrogen. Trans. Faraday Soc. 62, 3366–3374.

Colegrove, F.D., Hanson, W.B., Johnson, F.S., 1965. Eddy diffusion and oxygen transport in the lower thermosphere. J. Geophys. Res. 70, 4931–4941.

Connes, P., Noxon, J.F., Traub, W.A., Carleton, N.P., 1979. $O_2(^1\Delta)$ emission in the day and night airglow of Venus. Astrophys. J. 233, L29–L32.

Crisp, D., Meadows, V.S., Bézard, B., de Bergh, C., Maillard, J.P., Mills, F.P., 1996. Ground-based near-infrared observations of the Venus nightside: 1.27-μm O_2 ($a^1\Delta_g$) airglow from the upper atmosphere. J. Geophys. Res. 101, 4577–4593.

Dalgarno, A., Babb, J.F., Sun, Y., 1992. Radiative association in planetary atmospheres. Planet. Space Sci. 40, 243–246.

Drossart, P., Piccioni, G., Gérard, J.C., Lopez-Valverde, M.A., Sánchez-Lavega, A., Zasova, L., Hueso, R., Taylor, F.W., Bezard, B., Adriani, A., Angrilli, F., Arnold, G., Baines, K.H., Bellucci, G., Benkhoff, J., Bibring, J.P., Blanco, A., Blecka, M.I., Carlson, R.W., Coradini, A., Di Lellis, A., Encrenaz, T., Erard, S., Fonti, S., Formisano, V., Fouchet, T., Garcia, R., Haus, R., Helbert, J., Ignatiev, N.I., Irwin, P., Langevin, Y., Lebonnois, S., Luz, D., Marinangeli, L., Orofino, V., Rodin, A.V., Roos-Serote, M.C., Saggin, B., Stam, D.M., Titov, D., Visconti, G., Zambelli, M., Tsang, C., 2007. A dynamic upper atmosphere of Venus as revealed by VIRTIS on Venus Express. Nature 450, 641–645.

Fox, J.L., 1994. Rate coefficient for the reaction N + NO. J. Geophys. Res. 99, 6273–6276.

Gérard, J.C., Cox, C., Saglam, A., Bertaux, J.L., Villard, E., Nehmé, C., 2008a. Limb observations of the ultraviolet nitric oxide nightglow with SPICAV on board Venus Express. J. Geophys. Res. 113, E0003.

Gérard, J.C., Saglam, A., Piccioni, G., Drossart, P., Cox, C., Erard, S., Hueso, R., Sánchez-Lavega, A., 2008b. Distribution of the O_2 infrared nightglow observed with VIRTIS on board Venus Express. Geophys. Res. Lett. 35, L02207.

Gérard, J.C., Cox, C., Soret, L., Saglam, A., Piccioni, G., Bertaux, J.L., Drossart, P., 2009. Concurrent observations of the ultraviolet nitric oxide and infrared O_2 nightglow emissions with Venus Express. J. Geophys. Res. 114, E00B44.

Gérard, J.C., Stewart, A.I.F., Bougher, S.W., 1981. The altitude distribution of the Venus ultraviolet nightglow and implications on vertical transport. Geophys. Res. Lett. 8, 633–636.

Hedin, A.E., Niemann, H.B., Kasprzak, W.T., Seiff, A., 1983. Global empirical model of the Venus thermosphere. J. Geophys. Res. 88, 73–83.

Hueso, R., Sánchez-Lavega, A., Piccioni, G., Drossart, P., Gérard, J.C., Khatuntsev, I., Zasova, L., Migliorini, A., 2008. Morphology and dynamics of Venus oxygen airglow from Venus Express/visible and infrared thermal imaging spectrometer observations. J. Geophys. Res. 113, 542–552.

Hundsdorfer, W., Verwer, J.G., 2007. Numerical Solution of Time-Dependent Advection–Diffusion-Reaction Equations. Springer, Amsterdam.

Jacobson, M.Z., 2005. Fundamentals of Atmospheric Modeling. Cambridge University Press, New York.

Karniadakis, G.E., Kirby II, R.M., 2005. Parallel Scientific Computing in C++ and MPI. Cambridge University Press, New York.

Lellouch, E., Clancy, T., Crisp, D., Kliore, A., Titov, D., Bougher, S.W., 1997. Monitoring of mesospheric structure and dynamics. In: Bougher, S.W., Hunten, D.M., Philips, R.J. (Eds.), Venus II: Geology, Geophysics, Atmosphere, and Solar Wind Environment. The University of Arizona Press, Tucson.

Lellouch, E., Paubert, G., Moreno, R., Moullet, A., 2008. Monitoring Venus' mesospheric winds in support of Venus Express: IRAM 30-m and APEX observations. Planet. Space Sci. 56, 1355–1367.

Miller, H.C., McCord, J.E., Choy, J., Hager, G.D., 2001. Measurement of the radiative lifetime of $O_2(a^1\Delta_g)$ using cavity ring down spectroscopy. J. Quant. Spectrosc. Radiat. Transfer 69, 305–325.

Ohtsuki, S., Iwagami, N., Sagawa, H., Ueno, M., Kasaba, Y., Imamura, T., Nishihara, E., 2008. Imaging spectroscopy of the Venus 1.27-μm O_2 airglow with ground-based telescopes. Adv. Space Res. 41, 1375–1380.

Piccioni, G., Zasova, L., Migliorini, A., Drossart, P., Shakun, A., García Muñoz, A., Mills, F.P., Cardesin-Moinelo, A., 2009. Near-IR oxygen nightglow observed by VIRTIS in the Venus upper atmosphere. J. Geophys. Res. 114, E00B38.

Roble, R.G., Gary, J.M., 1979. The effect of horizontal transport on auroral NO densities. Geophys. Res. Lett. 6, 703–706.

Stewart, A.I.F., Gérard, J.C., Rusch, D.W., Bougher, S.W., 1980. Morphology of the Venus ultraviolet night airglow. J. Geophys. Res. 85, 7861–7870.

Yung, Y.L., Demore, W.B., 1982. Photochemistry of the stratosphere of Venus: implications for atmospheric evolution. Icarus 51, 199–247.

von Zahn, U., Fricke, K.H., Hoffmann, H.J., Pelka, K., 1979. Venus: Eddy coefficients in the thermosphere and the inferred helium content of the lower atmosphere. Geophys. Res. Lett. 6, 337–340.